Ceramics International 50 (2024) 31955–31965

Contents lists available at ScienceDirect

Ceramics International

journal homepage: www.elsevier.com/locate/ceramint

Blue pigment based on Ni-doped Zn_2GeO_4: Addressing structure and electronic properties by combining experiment and theory

Katiana L. Patrocínio [a], Gleison N. Marques [a], Amanda F. Gouveia [b,**], Lara K. Ribeiro [a], Nayara A. Pinheiro [a,c], Maria I.B. Bernardi [d], Lúcia H. Mascaro [a], Juan Andrés [b,***], Elson Longo [a], Marcelo Assis [b,*]

[a] CDMF, LIEC, Universidade Federal de São Carlos (UFSCar), São Carlos, 13565-905, Brazil
[b] Department of Physical and Analytical Chemistry, University Jaume I (UJI), Castelló, 12071, Spain
[c] NPE/LACOM, Universidade Federal da Paraíba (UFPB), João Pessoa, 58059-900, Brazil
[d] Physics Institute of São Carlos, University of São Paulo (IFSC-USP), São Carlos, 13560-970, Brazil

ARTICLE INFO

Handling Editor: Dr P. Vincenzini

Keywords:
Zn_2GeO_4
Blue pigments
Ni^{2+}-doping
DFT calculations

ABSTRACT

Understanding the process of color development and creating practical and efficient blue pigments is crucial in ceramics. The current work describes the synthesis and characterization of Ni^{2+}-doped Zn_2GeO_4 samples with varying concentrations (x = 0, 0.01, 0.02, 0.04, 0.08 and 0.16 mol%) as an effective strategy for tailoring their structure and electronic properties. These materials were synthesized using the coprecipitation method followed by microwave-assisted hydrothermal treatment at 140 °C for 10 min, and the as-synthesized samples underwent heat treatment at 1000 °C for 2 h to establish thermal-colorimetric stability. The synergistic effect of the Ni^{2+} 3d orbitals generating energy levels as new trapping sites in a broad energy range above the valence band was verified using DFT calculations. The substitution of Zn^{2+} by Ni^{2+} at x = 0.01 % changes the local electronic structure, resulting in a switchable electron transfer from the [NiO_4] and the neighbor [ZnO_4]and [GeO_4] tetrahedral clusters to shared oxygen anions, which is responsible for the observed blue color, as confirmed by colorimetric and spectroscopic analysis. This study paves the way, shedding light on the strategic design of a new class of ceramic pigments characterized by low toxicity, a vibrant blue hue, and excellent chemical/thermal durability. Furthermore, it provides a robust platform for exploring its potential application in the color-tunable Zn_2GeO_4-based materials.

1. Introduction

Blue pigments have garnered substantial attention due to their potential applications in visual arts and various industrial uses, primarily owing to their photo-absorption characteristics in the lower visible region [1]. Transition metals and rare earth elements doping processes have a longstanding history in the ceramic industry, offering a promising avenue for blue pigment development. Examples include YBO_3 doped with Mn cations for bluish-gray pigments used in building coatings to mitigate solar radiation absorption [2]. Environmentally friendly cold blue pigments have also been obtained from copper and strontium silicates doped with rare earth cations (Pr, Nd, and Sm) [3]. Despite the wide variety of blue pigments currently available, they typically require long periods of high-temperature heat treatment for the blue color to appear. Smith et al. [4], for example, produced a blue pigment using the $YIn_{1-x}Mn_xO_3$ matrix through a mixed oxide process (Y_2O_3, Mn_2O_3, and In_2O_3), which required an initial heat treatment of 12 h at 1200 °C. A similar synthesis method was used by Wang et al. to produce different shades of blue pigments from vanadium-zircon silicate (V–$ZrSiO_4$) after 5 h at a temperature of between 500 and 900 °C [5]. Other matrices, such as Zn_2SiO_4, also face problems with high-temperature synthesis [6]. Even so, the methods that sought to produce blue pigments using Zn_2SiO_4 in wet reactions observed the formation of powders with mixed phases in the precursors, once again leading to the need to use heat treatments for 12 h [7].

Zinc germanate, Zn_2GeO_4 (ZGO), stands out as a semiconductor due

* Corresponding author.
** Corresponding author.
*** Corresponding author.
E-mail addresses: gouveiad@uji.es (A.F. Gouveia), andres@qfa.uji.es (J. Andrés), marcelostassis@gmail.com (M. Assis).

https://doi.org/10.1016/j.ceramint.2024.05.493
Received 13 February 2024; Received in revised form 20 May 2024; Accepted 31 May 2024
Available online 2 June 2024

to its non-toxic properties, direct band gap excitation (around 4.4 eV), and straightforward synthesis across different scales [8,9]. This makes it an exceptional matrix for doping to create innovative pigments. As an inherently n-type semiconductor attributed to intrinsic donor defect states, ZGO finds diverse applications in photocatalysis for water splitting, pollutant degradation, photocatalytic hydrogen generation, luminescent thermometers, UV detectors, and beyond [10–12]. At room temperature, ZGO adopts a rhombohedral structure, capable of transforming into different structures under high pressures and temperatures. Its well-established optical properties, coupled with native defects and ionic solid bonds (Zn–O and Ge–O), induce local lattice distortions, generating electronic levels within the band gap [13–18]. Additionally, doping processes with cations of transition metals with suitable sizes and amounts to occupy the adequate sites of the ZGO have been widely used to promote optoelectronic performance and stability. In particular, Mn^{2+}-doped ZGO nanocrystals exhibit bright and green persistent emission [19,20]. Than et al. show that the bluish-white light emission of Cr^{3+} co-doped ZGO was synthesized using hydrothermal [21]. This indicates the feasibility of tailoring the optical properties of ZGO through controlled doping, opening avenues for diverse applications in optoelectronics and beyond.

Recent studies suggest a possible application in producing blue pigments using Co^{2+}-doped ZGO through the solid-state ceramic route [22]. However, the use of Co^{2+} faces notable challenges, such as its toxicity to humans and the environmental impacts associated with its mining [23,24]. Some authors have demonstrated that toxic concentrations for human cells obtained for Co^{2+} and Ni^{2+} can be up to three times lower for Co^{2+} compared to Ni^{2+} [25,26]. Ni^{2+} doping at ZGO is expected to confer a rich color to ceramic pigments via the $4s^2 3\ d^8$ configuration [22], depending on the concentration of Ni^{2+} cations and other elements in the host lattice [23,27–29]. Some ceramic matrices were doped with Ni^{2+} and showed excellent viability in terms of forming blue pigments. Very recently, Ni-Doped Zn_2SiO_4 blue pigments with high-NIR reflectance have been reported [30]. Costa et al. synthesized a turquoise-blue pigment based on Ni^{2+}-doped hibonite in a solid-state reaction, with potential applications in glazes and porcelain [31] Subsequently, Ianos et al. synthesized cold blue pigments based on Ni^{2+} and La^{3+}-doped hibonite through combustion [27]. Khairya et al. doped ZnO with Ni^{2+} cations using the coprecipitation method. They performed heat treatment at different temperatures, observing the attainment of various shades of blue and highlighting the direct influence of temperature [32].

In this work, we present an effective doping strategy involving a two-step facile coprecipitation method followed by microwave-assisted hydrothermal treatment at 140 °C for 10 min to synthesize Ni^{2+}-doped ZGO at different concentrations (x = 0–0.16 mol%). Furthermore, the synthesized samples underwent comprehensive characterization using various techniques, including X-ray diffraction (XRD) with Rietveld refinement, Raman spectroscopy, X-ray photoelectron spectroscopy (XPS), field emission scanning electron microscopy (FE-SEM), diffuse reflectance spectroscopy (DRS), diffuse reflectance spectroscopy (UV–vis), and colorimetry. To complement the experimental findings and systematically explore the structural evolution of Ni^{2+} in ZGO, density functional theory (DFT) calculations were undertaken to understand the local geometry and density of states (DOS) of Ni^{2+}-doped ZGO, particularly $[NiO_4]$ and the tetrahedral $[ZnO_4]$ and $[GeO_4]$ neighbor clusters. Our theoretical and experimental results provide deep insights into the colorimetric properties of Ni^{2+}-doped ZGO. This opens an exciting way to develop ZGO-based materials as blue pigments.

2. Materials and methods

2.1. Samples preparation

The ZGO samples were synthesized via the coprecipitation method followed by microwave-assisted hydrothermal treatment at 140 °C for 10 min [8,33,34]. For the pure sample, two separate aqueous solutions of metal precursors were prepared. The first solution contained zinc nitrate hexahydrate (2 mmol, $Zn(NO_3)_2{\cdot}6H_2O$ - Chem Impex Inc, 99.84 %), while the second was prepared using germanium oxide (1 mmol, GeO_2 - Sigma Aldrich, 99.99 %). These solutions were then mixed under continuous stirring and heated to 70 °C. Subsequently, the pH was adjusted to 10 by adding NaOH, with continuous stirring until a suspension formed, which typically took around 15 min. At basic pH, GeO_2 forms the GeO_3^{2-} ion, capable of interacting with Zn^{2+} ions in basic solution, as shown below:

$$GeO_2 + 2OH^- \rightarrow GeO_3^{2-} + H_2O \quad \text{(Eq. 1)}$$

$$Zn(NO_3)_2.6H_2O \rightarrow Zn^{2+} + 2NO_2^- + 6H_2O \quad \text{(Eq. 2)}$$

$$2Zn^{2+} + GeO_3^{2-} + 2OH^- \rightarrow Zn_2GeO_4 + H_2O \quad \text{(Eq. 2)}$$

The mixture was then transferred to a Teflon reactor and subjected to microwave irradiation at 140 °C for 10 min, using 2.45 GHz and power of 800 W, resulting in the formation of a white precipitate. After this step, the residue was subjected to several washes with deionized water and centrifuged to remove residual ions.

In the synthesis of Ni-doped ZGO, the synthesis process was similar, with the difference that nickel nitrate hexahydrate ($Ni(NO_3)_2{\cdot}6H_2O$ - Sigma Aldrich, 99 %) was also added to the zinc nitrate solution in proportions ranging from 0.01 % to 0.16 %. For this, the following amounts were added: for 0.01 % Ni^{2+} doping, 1.98 mmol of $Zn(NO_3)_2{\cdot}6H_2O$ and 0.02 mmol of $Ni(NO_3)_2{\cdot}6H_2O$; for 0.02 % Ni^{2+} doping, 1.96 mmol of $Zn(NO_3)_2{\cdot}6H_2O$ and 0.04 mmol of $Ni(NO_3)_2{\cdot}6H_2O$; for 0.04 % Ni^{2+} doping, 1.92 mmol of $Zn(NO_3)_2{\cdot}6H_2O$ and 0.08 mmol of $Ni(NO_3)_2{\cdot}6H_2O$; for 0.08 % Ni^{2+} doping, 1.84 mmol of $Zn(NO_3)_2{\cdot}6H_2O$ and 0.16 mmol of $Ni(NO_3)_2{\cdot}6H_2O$; and for 0.16 % Ni^{2+} doping, 1.68 mmol of $Zn(NO_3)_2{\cdot}6H_2O$ and 0.32 mmol of $Ni(NO_3)_2{\cdot}6H_2O$.

After adding Ni^{2+} cations, a color modification was observed, initially changing from white to a greenish hue. These samples underwent heat treatment at 1000 °C for 2 h to investigate the thermal-colorimetric stability of the produced powders. The samples of pure, doped with 0.01 %, 0.02 %, 0.04 %, 0.08 %, and 0.16 % Ni^{2+} were named ZGO, $Zn_{1.98}Ni_{0.02}GeO_4$ (ZGO1), $Zn_{1.96}Ni_{0.04}GeO_4$ (ZGO2), $Zn_{1.92}Ni_{0.08}GeO_4$ (ZGO4), $Zn_{1.84}Ni_{0.16}GeO_4$ (ZGO8), and $Zn_{1.68}Ni_{0.32}GeO_4$ (ZGO16), respectively, while the samples subjected to thermal treatment were referred to as ZGO-1000, ZGO1-1000, ZGO2-1000, ZGO4-1000, ZGO8-1000 and ZGO16-1000, respectively.

2.2. Characterizations

The obtained samples underwent a structural analysis using various characterization techniques. The XRD method used a DMax2500PC diffractometer (Rigaku, Japan). Rietveld refinement was employed using the GSAS software and the EXPGUI interface to obtain accurate information on phase percentages and data on the unit cell parameters. Raman spectroscopy was conducted using a T64000 spectrometer (Horiba Jobin – Yvon, Japan) coupled with a Synapse CCD and an argon ion laser detector operating at 633 nm, providing structural data. Fourier-transform infrared spectroscopy (FTIR) analysis was performed on a Bomem-Michelson spectrophotometer, using the transmittance mode (model MB102) in the range of 250–1000 cm^{-1}, employing KBr pellets as a reference. The morphology of the samples was assessed using an FE-SEM Supra 35-VP microscope operating at 5 kV. Elemental composition distributions of the samples were evaluated using energy-dispersive spectroscopy (EDS), operating at 20 kV in BSE mode, coupled to a scanning electron microscope (Hitachi, TM4000 Plus). XPS measurements were conducted utilizing an ESCA spectrometer (Scientia Omicron, Germany) equipped with a monochromatic X-ray source of Al Kα (1486.7 eV). The binding energies of all elements were adjusted about the C 1s peak at 284.8 eV. Diffuse reflectance measurements were

obtained using a Varian Cary model 5G spectrometer in the diffuse reflectance mode, with a wavelength range of 200–1800 nm and a scan speed of 600 nm min^{-1}.

For the analysis of colorimetric coordinates of the acquired powders, a Minolta spectrophotometer, model CM2600d, was used with a wavelength range between 400 and 700 nm. The equipment had a standard D65-type light source (daylight), following CIELab (International Commission of I'Eclairage - CIE) standards. The color difference between the powders was determined using Equation (2), considering the values of the colorimetric coordinates. These coordinates include Luminosity (L, ranging from 0 for black to 100 for white), a* (positive values indicate red, negative values indicate green), and b* (positive values indicate blue, negative values indicate yellow).

2.3. Theoretical calculations

First-principles calculations for ZGO and Ni-doped ZGO (Ni-ZGO) models were performed using the CRYSTAL17 software package [35,36]. The computational methods are based on the DFT calculations at the B3LYP hybrid functional level were performed [37,38]. The diagonalization of the Fock matrix was performed using an adequate number of k-point grids in the reciprocal space. The thresholds controlling the accuracy of the Coulomb and exchange integrals calculations were set to 1×10^{-8} and 1×10^{-16}, respectively, and the percentage of Fock/Kohn-Sham matrix mixing was set to 30. The Zn, Ge, Ni, and O atomic centers were described by 86-411d31G, DURAND-21G*, 86–411 (41d)G, and 6-31d1 basis sets, respectively. These were obtained from the CRYSTAL website [39]. The lattice parameters and internal atomic coordinates of the ZGO were fully optimized until all force components were less than 10^{-6} eV $Å^{-2}$.

The unit cell of the ZGO is composed of a six-unit formula (Z = 6) formed by $[ZnO_4]$ and $[GeO_4]$ clusters. Moreover, this structure contains two types of six-membered rings and one type of four-membered ring, in which two types of non-equivalent Zn sites (Zn1 and Zn2) can be sensed, as shown in Fig. 1a. A kind of six-membered ring is built by alternately corner-shared $[ZnO_4]$ and $[GeO_4]$ clusters with the Zn1 atoms, and the other is composed of corner-shared $[ZnO_4]$ clusters with only Zn2 atoms. The four-member ring is built by alternately corner-shared $[ZnO_4]$ clusters (Zn1 and Zn2) and $[GeO_4]$ clusters. For the modeling of the Ni-ZGO, a $1 \times 1 \times 1$ supercell periodic model was constructed, being geometrically optimized. A complete exploration of the possible substitution sites of Zn1 or Zn2 by Ni^{2+} cation has been performed. The results show that the more energetically favorable substitution occurs in Zn2 (see Fig. 1a). Unfortunately, achieving lower percentages of Ni^{2+} doping would necessitate using a larger supercell model, rendering it cost-prohibitive due to increased computational expenses.

3. Results and discussion

XRD patterns of ZGO and ZGO1 powders (with and without temperature treatment) are shown in Fig. 2. All Bragg peaks are indexed to a rhombohedral structure with the R-3 space group, card number 68382 in the Inorganic Crystal Structure Database (ICSD) reveals the lattice parameters as a = b = 14.2841 Å and c = 9.5471 Å. Notably, no secondary phase was detected, confirming the high purity of the samples. The crystalline structure of ZGO comprises corner-sharing tetrahedral $[ZnO_4]$ and $[GeO_4]$ clusters, bridged by oxygen anions, arranged in a pattern parallel to the c-axis [14,15,17,40]. Conversely, the ZGO16 samples are composed of three different phases: the rhombohedral structure of ZGO, NiO with a cubic structure and Fm-3m space group (ICSD 9866), and the $Zn_{1.2}Ni_{0.8}GeO_4$ with a cubic structure and Fd-3m space group (ICSD 69519). Notably, a lower range of x = 0.16 % Ni^{2+}-doping was synthesized, and the blue color was maintained.

Analyzing the most intense peak (410) of the Zn_2GeO_4 phase in all samples, a shift to higher 2θ values is observed, indicating a contraction of the material's crystal lattice when doped with Ni^{2+}. There is also a variation in the peak's total width values at half maximum (FWHM) (410). The FWHM values for the samples without thermal treatment are 0.434°, 0.432°, and 0.374° for ZGO, ZGO1, and ZGO16, respectively. This reduction in FWHM values suggests an increase in long-range structural ordering. However, when compared to the thermally treated samples, it is observed that the FWHM values are 0.143°, 0.149°, and 0.180° for ZGO-1000, ZGO1-1000, and ZGO16-1000, respectively. Therefore, Ni^{2+} doping increases long-range structural ordering at low

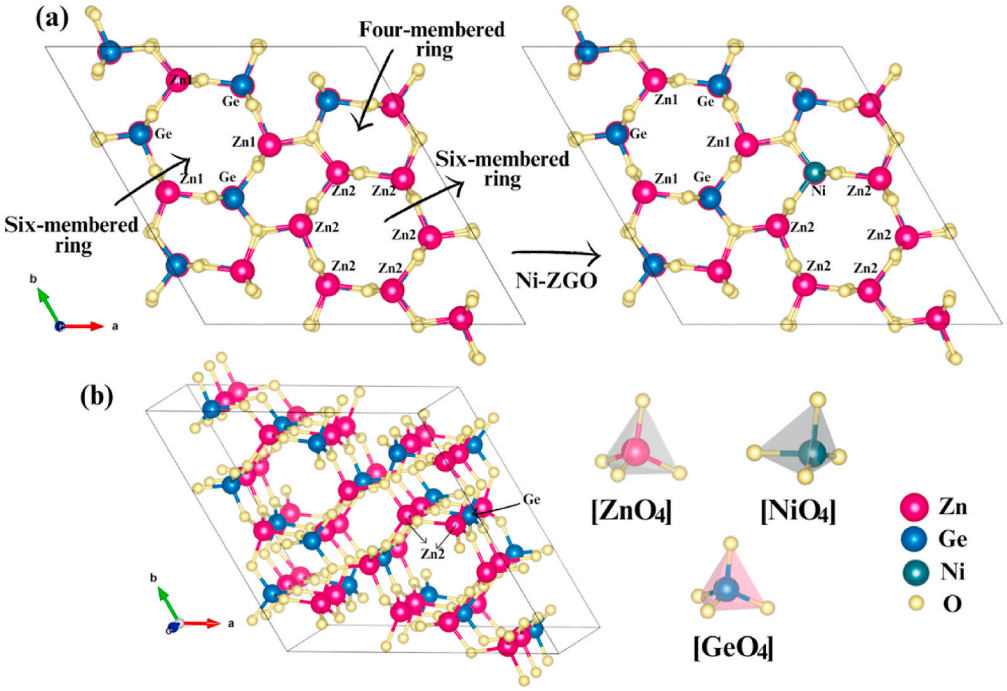

Fig. 1. **(a)** ZGO structure is composed of the six- and four-membered rings involving the $[ZnO_4]$ and $[GeO_4]$ clusters. The most energetically favorable Ni^{2+}-doping process occurs at the Zn2 site. **(b)** 3D view of the ZGO structure and the $[ZnO_4]$, $[NiO_4]$, and $[GeO_4]$ clusters.

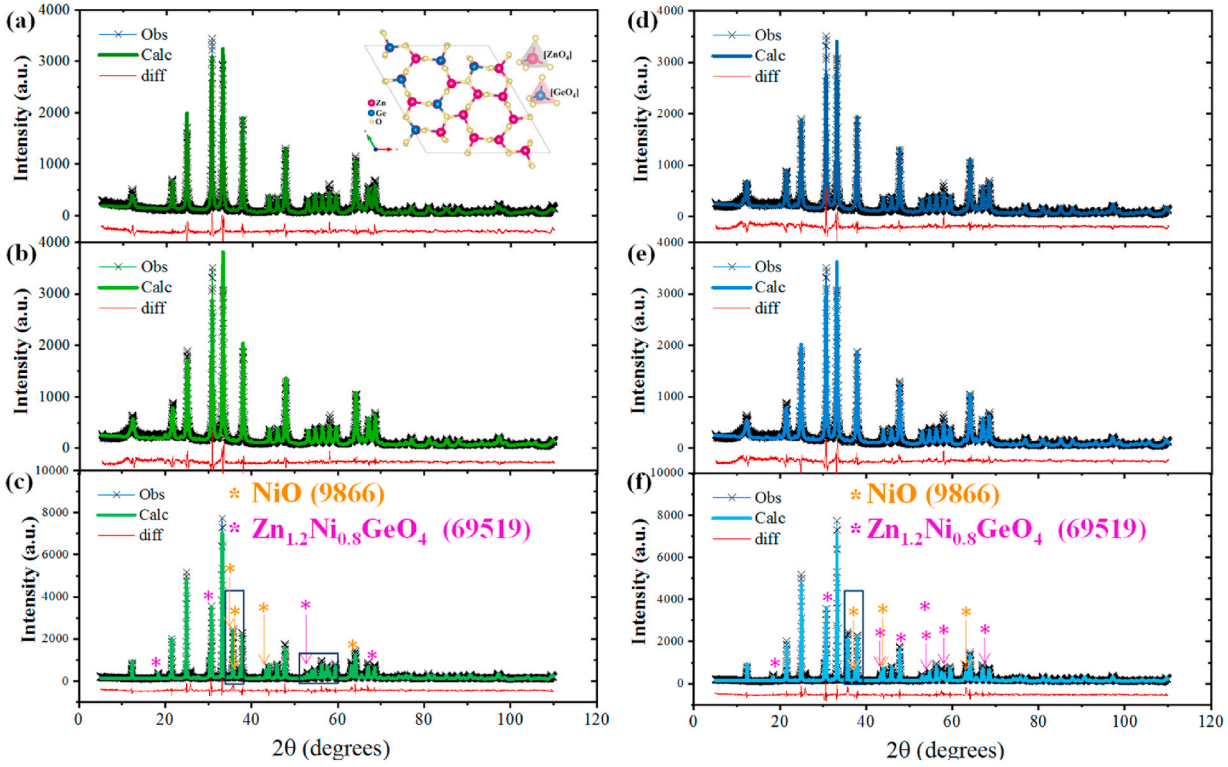

Fig. 2. XRD and Rietveld refinements of the samples. **(a)** ZGO; **(b)** ZGO1; **(c)** ZGO16; **(d)** ZGO-1000; **(e)** ZGO1-1000; and **(f)** ZGO16-1000.

temperatures, but at high temperatures, this process results in a more disordered system with the appearance of new defects.

Rietveld refinements of the samples were conducted to understand better the structural modifications provoked by the Ni^{2+} doping process and thermal treatment (Table 1). For all samples, the refinement quality, as indicated by the χ^2 values, suggests that Ni^{2+} substitution occurs at the Zn^{2+} sites. For samples without thermal treatment, Ni^{2+} doping reduces the lattice parameters and, consequently, decreases the volume of the crystal unit cell of ZGO. In contrast, the opposite effect is observed for thermally treated samples. These results are consistent with the peak shift (410) observed in the XRD analysis. The compositional analysis of ZGO16 renders the pure ZGO (~89 %), NiO (~3 %), and $Zn_{1.2}Ni_{0.8}GeO_4$ (~8 %). Both the diffractograms and the compositional analysis by Rietveld of Ni-doped ZGO samples with intermediate compositions of 0.02, 0.04, and 0.08 % are shown in Fig. S1 and Table S1. For untreated samples, it is not observed the formation of secondary phases, in contrast to thermally treated samples, which only show secondary phase at 8 % ($Zn_{1.2}Ni_{0.8}GeO_4$). Moreover, the ZGO structure was optimized, and the calculated equilibrium lattice parameters agree with the experimental values, as reported in Table 1. The DFT values differ by less than 1 % from the experimental values (0.8 % and 0.6 % for the a and c lattice parameters, respectively). For comparison purposes, the values of the previously calculated lattice parameters in the literature are reported in Table S2, and more minor deviations of 1 % are observed [41–44]. Table S3 presents the calculated values of bond distances and angles of ZGO and Ni-ZGO. The Zn–O and Ge–O bonds of [ZnO_4] and [GeO_4] neighbor clusters increased slightly, 2.2 % and 1.2 %, respectively, while the Ni–O bond distances decreased by 8.9 % and 6.2 % for the O bond shared with Zn and Ge atoms, respectively. Moreover, the bond angles in the O–Zn–O and O–Ge–O decreases by 3.9 % and 1.6 %, respectively, while the O–Ni–O bond angles increase by +18.6 %.

Table 1
Structural results obtained from Rietveld refinements and theoretical simulations.

Samples		Lattice parameters (Å)		Cell Volume (Å^3)	χ^2	Phase Fraction%
		a = b	c			
ZGO Theo	Zn_2GeO_4	14.401	9.631	1729.645		
ZGO	Zn_2GeO_4	14.285	9.571	1691.587	3.64	100
ZGO-1	Zn_2GeO_4	14.242	9.540	1675.985	3.80	100
ZGO-16	Zn_2GeO_4	14.255	9.543	1679.678	4.44	88.6
	NiO	4.168	4.168	72.434		3.10
	$Zn_{0.2}N_{0.8}GeO_4$	8.330	8.330	578.130		8.30
ZGO-1000	Zn_2GeO_4	14.273	9.560	1686.846	3.69	100
ZGO-1-1000	Zn_2GeO_4	14.280	9.555	1687.459		100
ZGO-16-1000	Zn_2GeO_4	14.256	9.544	1680.000	4.47	89.0
	NiO	4.167	4.167	72.394		2.40
	$Zn_{0.2}N_{0.8}GeO_4$	8.332	8.332	578.458		8.60

Raman and FTIR spectroscopies are crucial tools for analyzing the effects of short-range order and disorder in crystalline solids, complementing XRD analysis (Fig. 3). For all samples, Raman modes in the range of 700–850 cm^{-1} were identified (Fig. 3a) [45]. For the ZGO sample, 4 active Raman modes were observed, namely: 740 cm^{-1} (A_g), 747 cm^{-1} (E_g), 769 cm^{-1} (E_g), and 796 cm^{-1} (A_g), related to the stretching of Zn–O and Ge–O bonds and bending modes of Ge–O–Zn of the [ZnO_4] and [GeO_4] clusters [12,46,47]. For sample ZGO1, these active Raman modes were observed with slight modifications. In sample ZGO16, the absence of the 770 cm^{-1} mode was noted. After thermal treatment, an increase in the intensity and definition of Raman modes is observed, which can be associated with the increased crystallinity achieved through the thermal treatment. Table S4 presents the obtained values and previously reported literature on the active Raman modes of the rhombohedral ZGO structure. A comparison shows that the difference is less than 1 % [15,47].

To better understand the changes in intensity and the loss of definition in the Raman modes of the samples, an analysis of the FWHM of

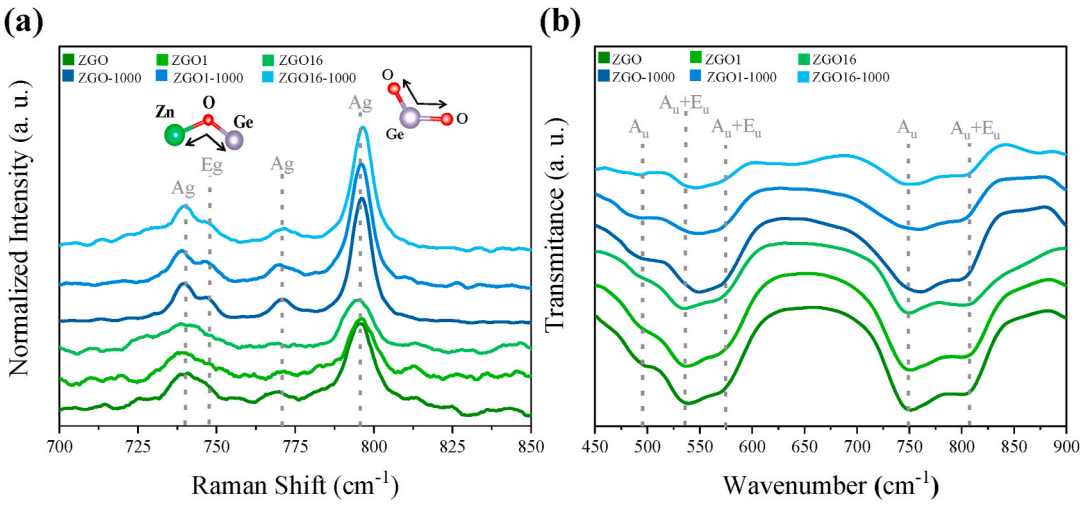

Fig. 3. **(a)** Raman spectra and **(b)** FTIR spectra of the samples.

the highest-intensity mode, located at ~796 cm^{-1}, was conducted. The results obtained for the ZGO, ZGO1, and ZGO16 samples were 10.4, 10.4, and 12.2 cm^{-1}, respectively. The calculation of the FWHM for this same mode in samples subjected to thermal treatment resulted in values of 7.6, 8.2, and 8.2 cm^{-1} for the ZGO-1000, ZGO1-1000, and ZGO16-1000 samples, respectively. This difference observed in the FWHM values could be attributed to an increase in the degree at short-range caused by the increase of Ni^{2+}.

The FTIR analysis was conducted, focusing on the region between 400 and 900 cm^{-1}, as this range allows the identification of vibrations related to metal-oxygen bonds (Fig. 3b). For Zn_2GeO_4, nine active vibrational modes (A_u and E_u) can be identified in the infrared spectrum, where A_u modes exhibit polarization along the crystallographic z-axis. In contrast, E_u modes degenerate in the rhombohedral xy plane [48]. It is possible to observe five bands in this region for the samples synthesized in this work. Between 400 and 600 cm^{-1}, the modes associated with the symmetric stretching of the O–Zn–O bonds can be observed, with peaks at 493 (A_u), 536 ($A_u + E_u$), and 576 cm^{-1} ($A_u + E_u$). In the region between 600 and 900 cm^{-1}, modes corresponding to the asymmetric stretching of the O–Ge–O bonds are found, with peaks at 748 cm^{-1} (A_u) and 808 cm^{-1} ($A_u + E_u$) [49–53]. As FTIR is not an analysis sensitive to local symmetry like Raman, significant changes are not observed between the samples. For samples with intermediate concentrations (0.02, 0.04, and 0.08 %), the same trend is observed in both Raman spectroscopy and FTIR spectra (see Fig. S2).

The impact on the morphology of the as-synthetized samples was analyzed by FE-SEM (Fig. 4). For the samples without thermal treatment, it is observed that all are formed by nanorods, according to previous results in other studies [21,54]. The ZGO, ZGO1, and ZGO16 samples have average widths and lengths of 47.00 nm and 195.46, 54.47 nm and 195.39, and 62.61 nm and 175.44, respectively, noting that the increase in Ni^{2+} concentration induces an increase in nanorod width. After thermal treatment, the particles undergo a quasi-sintering process, significantly increasing their grain size and changing from nanorods to forming irregular polyhedrons, as reported in another study [50]. For the ZGO16-1000 sample, the formation of micro rods and cubes, likely induced by secondary phases, can be observed. ZGO-1000 and ZGO1-1000 samples present irregular polyhedrons with an average size of 645.43 nm and 491.73 nm, respectively. On the other hand, the ZGO16-1000 sample displays distinct morphologies due to different phases, where smaller structures have an average size of 139.92 nm, and rod-shaped particles have average widths and lengths of 51.16 nm and 256.12 nm. The thermal treatment induces a decrease in particle size and more pronounced morphological changes as the amount of increase in Ni^{2+} is increased. The SEM images related to the intermediate samples (0.02, 0.04, and 0.08 %) are shown in Fig. S3 and follow the same trend observed previously.

The elemental surface mapping of the samples by EDS was performed

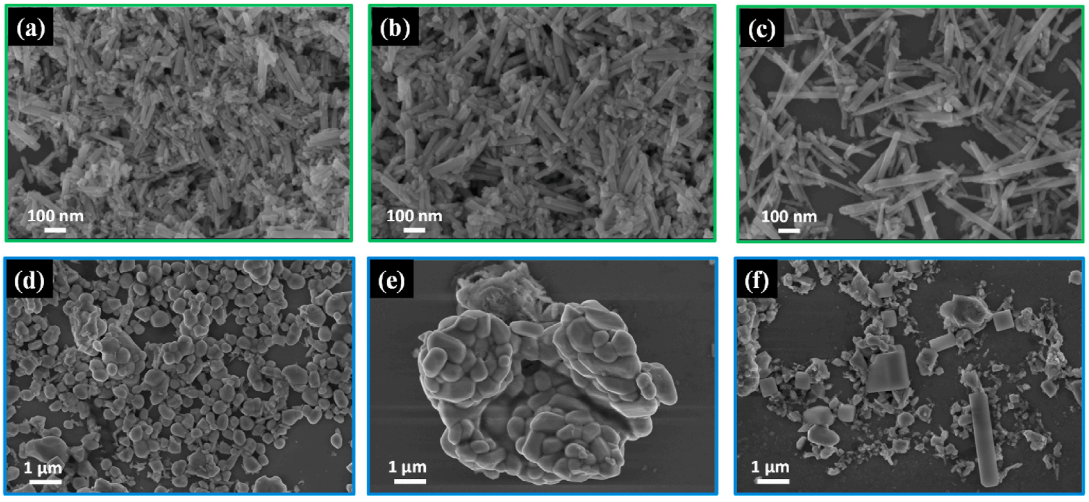

Fig. 4. FE-SEM images of the samples **(a)** ZGO, **(b)** ZGO1, **(c)** ZGO16, **(d)** ZGO-1000, **(e)** ZGO1-1000, and **(f)** ZGO16-1000.

after thermal treatment, as shown in Fig. S4. As these samples were obtained from samples without thermal treatment, the Ni content in both is equal. Zn, Ge, and O were identified in all samples, with Ni observed only in the doped samples. Although EDS analysis is partially quantitative, and its interpretation depends on the material's surface characteristics, the uniform detection of Ni throughout the sample and its quantification close to nominal (x = 0.01 and 0.16 %) reinforce that all the Ni added during synthesis is present in the sample.

XPS was employed to perform a detailed surface evaluation to examine the effects of Ni^{2+} doping and heat treatment on the ZGO samples. Fig. 5 presents the XPS spectra for Ge 3d, Zn 2p, O 1s, and Ni 2p, respectively. These high-resolution spectra confirm the existence of elements constituting the Zn_2GeO_4 structure, providing evidence for the successful formation of the material.

In Fig. 5a, the Ge 3d peaks reveal binding energies centered around 31 eV, indicative of the presence of Ge^{2+} state oxidation, while around 32 and 33 eV bonds are associated with the tetravalent form of Ge^{4+} [55–57]. One insight from XPS about Ge 3d is that the thermal treatment applied to the ZGO-1000 and ZGO1-1000 samples influenced the binding energy of the Ge 3d orbital. The shift towards lower energy values implies the potential development of stronger bonds between Ge and O within the crystal lattice. This observation underscores the substantial influence of heat treatment on structural alterations, as supported by the FWHM of the (410) peak in the XRD results, indicating a reduction in values for the heat-treated ZGO samples. While the diminishing FWHM suggests a long-range structural order, it is noteworthy that the ZGO16-1000 sample does not exhibit changes in the Ge 3d binding energy. This discrepancy can be attributed to the doping-induced, more significant long-range structural disorder and the appearance of new phases, preventing a shift towards lower binding energy in this specific case.

In Fig. 5b, high-resolution XPS spectra reveal binding energy peaks at 1022 and 1045 eV, corresponding to the Zn $2p_{3/2}$ and Zn $2p_{1/2}$ states, respectively. These peaks demonstrate the oxidation state of Zn^{2+} [58]. Fitted high-resolution XPS spectra of the O 1s region (Fig. 5c) reveal a peak in the binding energy range between 529 and 530 eV, attributed to the crystal lattice oxygen (O^{2-}) constituents of Ge–O bonds [55,59]. Furthermore, peaks in the 531 eV and 532 eV are observed, associated with the presence of oxygen hydroxyl groups and the surface adsorption of water molecules.

Due to the lower doping concentration, the Ni^{2+} peaks are notably absent in ZGO1 and ZGO1-1000 materials, as illustrated in Fig. 5d [60]. In contrast, for the ZGO16 and ZGO16-1000 samples, Ni $2p_{3/2}$ and Ni $2p_{1/2}$ peaks become evident at binding energies of 856.3 eV and 872.5 eV, respectively. These peaks correspond to the presence of Ni^{2+} cations within the material. An interesting fact for the heat-treated samples: apparently, there is a migration of Ni^{2+} from the surface to the bulk. This is known because the same sample was used for both processes, and the elemental distribution revealed by EDS mapping shows a homogeneous distribution, with quantitative analysis close to nominal values. In this way, the surface composition of ZGO can likely be altered through heat treatment, making it an intriguing process for the design of new

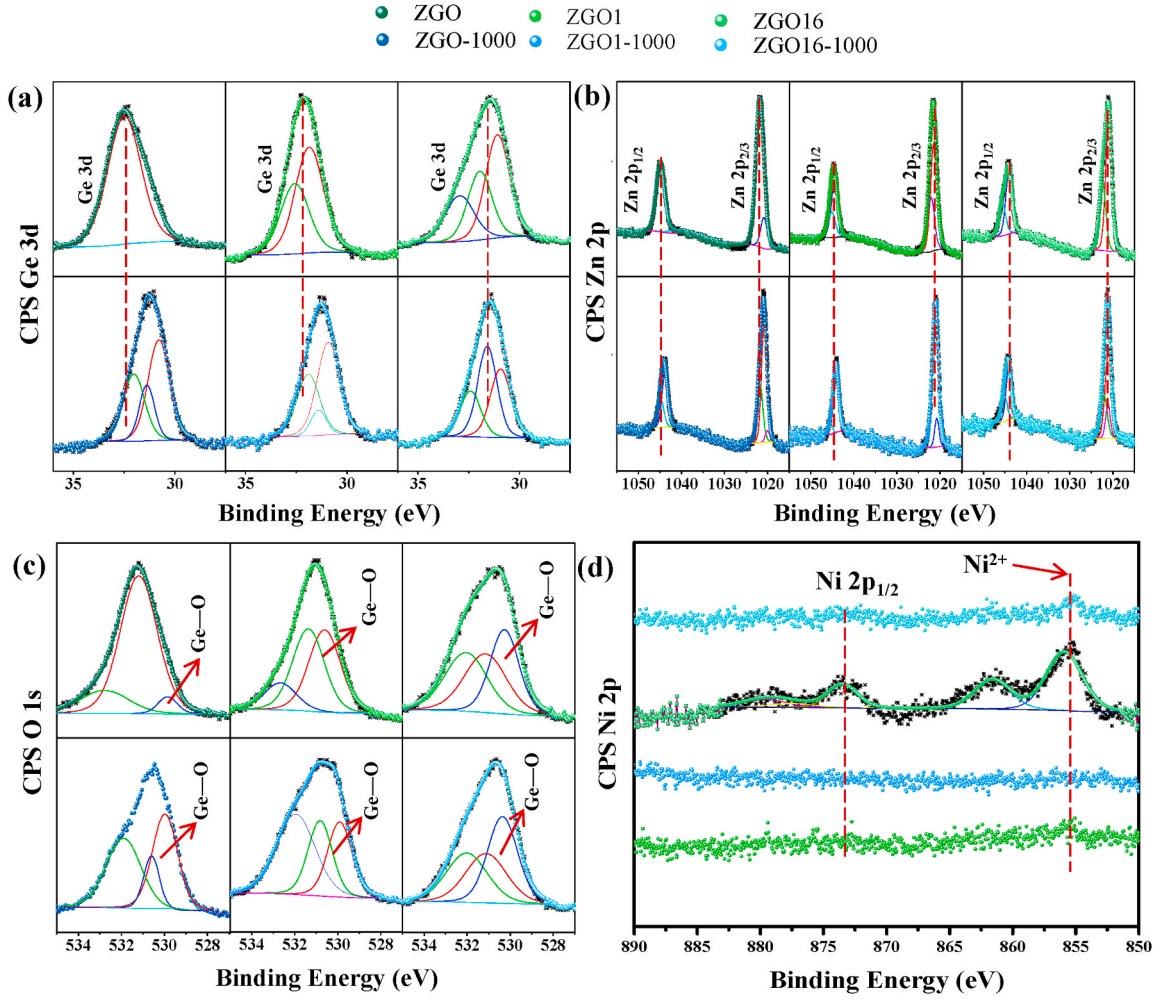

Fig. 5. Ge 3d XPS spectra of the ZGO samples (a). Zn 2p XPS spectra of the ZGO samples (b). O 1s XPS spectra of the ZGO samples (c). Ni 2p XPS spectra of Ni^{2+}-doped ZGO samples.

ZGO-based materials.

The changes in electronic properties caused by Ni^{2+} doping in the samples, both before and after thermal treatment, were analyzed by DRS. Reflectance spectra were used to calculate the optical band gap energies (E_{gap}) using the Wood-Tauc and Kubelka-Munk equations [61]. Previous studies indicate that Zn_2GeO_4 exhibits a band gap with direct transitions [13,21,33]. In Figs. S5a–c, representing the samples without thermal treatment, an E_{gap} of 4.76 eV is observed for ZGO, while ZGO1 and ZGO16 show E_{gap} values of 4.77 and 4.69 eV, respectively, with no significant changes. In Figs. S5d–f, representing the samples after thermal treatment, the appearance of the additional band gaps is observed, in agreement with previous literature [62]. The E_{gaps} for the ZGO-1000 sample were 3.16 eV and 4.45 eV, for ZGO1-1000 were 3.40 eV and 4.08 eV, and for ZGO16-1000 were 3.40 eV and 3.92 eV. The E_{gap} values of the intermediate samples follow the trend observed for the samples with and without thermal treatment, and are shown in Fig. S6. From these values, we can draw two conclusions: (1) thermal treatment induces the appearance of new, well-defined electronic transitions due to changes in short- and long-range order in the materials, and (2) Ni^{2+} doping in a highly structurally organized crystal lattice (due to thermal treatment) also induces the creation of intermediate levels in the forbidden region due to the generation of new local defects caused by Ni^{2+}-doping and the acquisition of new phases.

The DOS plot for ZGO is displayed in Fig. 6a. An analysis of the results renders that the valence band maximum (VBM) is mainly composed of Zn (d) and O (p) orbitals. In contrast, the conduction band minimum (CBM) is dominated by a hybridization of Zn(s), Ge(s), and O (p) orbitals. The electronic transition between the VBM and CBM presents an E_{gap} value of 4.57 eV. It is a direct transition at the Γ-point in the Brillouin zone, in agreement with the experimental value. To understand how the Ni^{2+}-doping process modulates the electronic structure of ZGO, the DOS of the Ni-ZGO was further analyzed, as illustrated in Fig. 6b. The top of the VBM is now mainly composed of 3d Ni orbitals and 2p O orbitals, and a strong hybridization between them, with a minor contribution from the Zn and Ge orbitals, and a decrease of the band gap value is observed (E_{gap} = 2.68 eV). On the other hand, a detailed analysis of DOS projected at the 3d orbitals of Ni was performed. As can be seen at Fig. S7, the 3d Ni^{2+} orbitals are non-degenerated, and the top of the VB is constituted by the $3d_{x^2-y^2}$ followed by $3d_{xy}$ with a smaller contribution of $3d_{z^2}$. This fact results in shallow traps and improved carrier separation.

The values of Mulliken atomic charges values are listed in Table 2. An analysis and comparison of ZGO and Ni-ZGO models show that the presence of Ni^{2+} cations induce an increase in the negative charge of O anions belonging to the $[NiO_4]$ cluster. There is a decrease of the positive charge of a neighbor $[GeO_4]$ cluster, from 0.46e to 0.37e, while the substituted site at $[ZnO_4]$ cluster, with a negative charge of −0.23e, increases its positive charge to 0.13e when is replaced by $[NiO_4]$ cluster in the doping process. Therefore, $[NiO_4]$ and neighbor $[GeO_4]$ and $[ZnO_4]$ clusters are the sites where positive and negative charges, respectively, are accumulated after the Ni^{2+}doping process. Therefore, we suggest that the true driving force to facilitate this charge separation and electronic flow from the $[NiO_4]$ and neighbor $[GeO_4]_{neighbor}$ and $[ZnO_4]_{neighbor}$ clusters to shared oxygen anions behavior is responsible for the appearance of blue color as it is depicted in Fig. 7.

The DRS of the samples in the ultraviolet–visible region (between 200 and 800 cm^{-1}) and near-infrared, NIR (800–1800 cm^{-1}) are shown in Fig. 8. For the samples without thermal treatment (Fig. 8a), it is observed that the ZGO and ZGO1 samples do not exhibit any absorption in the visible range, resulting in no coloration. In sample ZGO16, it is possible to identify two distinct bands: a prominent band located between 350 and 500 cm^{-1} and a broader band spanning the range of 500–800 cm^{-1}. For the samples after thermal treatment (Fig. 8b), it is noted that the ZGO-1000 sample does not show any absorption, imparting the expected white color. However, for the ZGO1-1000 and ZGO16-1000 samples, absorptions in the visible range are observed. The same behavior is observed for the samples with intermediate concentrations of 0.02, 0.04, and 0.08 % (Fig. S8). In the ZGO16, ZGO1-1000 and ZGO16-1000, two overlapping bands are observed in the range of 500–670 nm, The d-d transitions associated with the permitted configurations of the Ni^{2+} ion coordinated tetrahedrally include the states $^3A_2$ (^3P), ^3E (^3P), $^1T_2$ (^1G), $^1A_1$ (^1G), and $^1T_1$ (^1G) [25]. Additionally, a weak broadband in the range of 600–800 nm is observed, corresponding to the allowed spin transitions v_2 ($^3A_{2g} \rightarrow {}^3T_{1g}$ (F)) of the Ni^{2+} ion coordinated octahedrally [63,64]. With the increase in Ni^{2+} concentration, a prominent band emerges in the spectral range of 380 nm to approximately 400 nm, indicating charge transfer between oxygen (O), zinc (Zn), and nickel (Ni) atoms [63].

Specifically, the band at 400 nm is observed in the sample with 0.16 % Ni^{2+}, attributed to allowed spin transitions of Ni^{2+} at the octahedral sites ($^3A_2 \rightarrow {}^3T(F)$). Additionally, it is noteworthy the presence of two weak bands between 710 and 780 nm in the samples with 0.01 % and 0.16 % Ni^{2+}. At 710 nm, the transition $^3T_{1g}$ (^3F) occurs with the Ni^{2+} ion coordinated octahedrally, while at 780 nm, the transitions ^1E (^1D) and $^1T_2$ (^1D) occur with the Ni^{2+} ion coordinated tetrahedrally [27]. In the NIR region, two broad and overlapping bands in the 850–1300 nm range are also observed for the Ni^{2+}-doped samples, attributed to allowed spin transitions $^3A_{2g} \rightarrow {}^3T_{2g}$ (F). This absorption in the NIR can be of interest

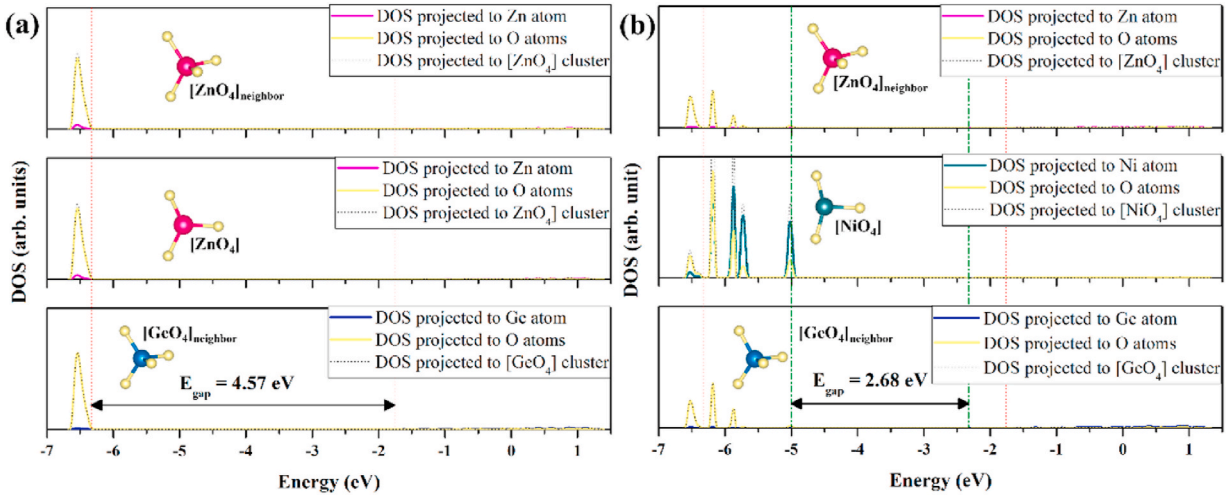

Fig. 6. **(a)** DOS projected onto the atoms within the $[ZnO_4]_{neighbor}$, $[ZnO_4]$ that was replaced by Ni^{2+} cation, and $[GeO_4]_{neighbor}$ clusters at the ZGO model. **(b)** DOS projected onto the atoms within the $[ZnO_4]_{neighbor}$, $[NiO_4]$, and $[GeO_4]_{neighbor}$ clusters at the Ni-ZGO model.

Table 2
Calculated Mulliken charges of Zn, O, Ge, and Ni atoms and $[ZnO_4]_{neighbor}$, $[GeO_4]_{neighbor}$, $[ZnO_4]$ that was replaced by Ni^{2+} cation, and $[NiO_4]$ clusters.

	$Zn_{neighbor}$	O	$Ge_{neighbor}$	O	Zn	Ni	O
ZGO	1.03	− 0.95 (O3)	1.72	− 0.95 (O1)	1.03	–	− 0.94 (O2)
		− 0.94(O4)		− 0.94 (O4)			− 0.95 (O3)
		− 0.94 (O2′)		− 0.94 (O2′)			− 0.95 (O4)
		− 0.94 (O2)		− 0.95 (O3)			− 0.94 (O2″)
Ni-ZGO	1.00	− 0.95 (O3)	1.66	− 0.94 (O1)	–	1.49	− 1.04 (O2)
		− 0.94 (O4)		− 0.93 (O4)			− 1.04 (O3)
		− 0.94 (O2′)		− 0.94 (O2′)			− 0.99 (O4)
		− 1.04 (O2)		− 1.04 (O3)			− 1.00 (O2″)

	$[ZnO_4]_{neighbor}$	$[GeO_4]_{neighbor}$	$[ZnO_4]$	$[NiO_4]$
ZGO	− 0.23	0.46	− 0.23	–
Ni-ZGO	− 0.28	0.37	–	0.13

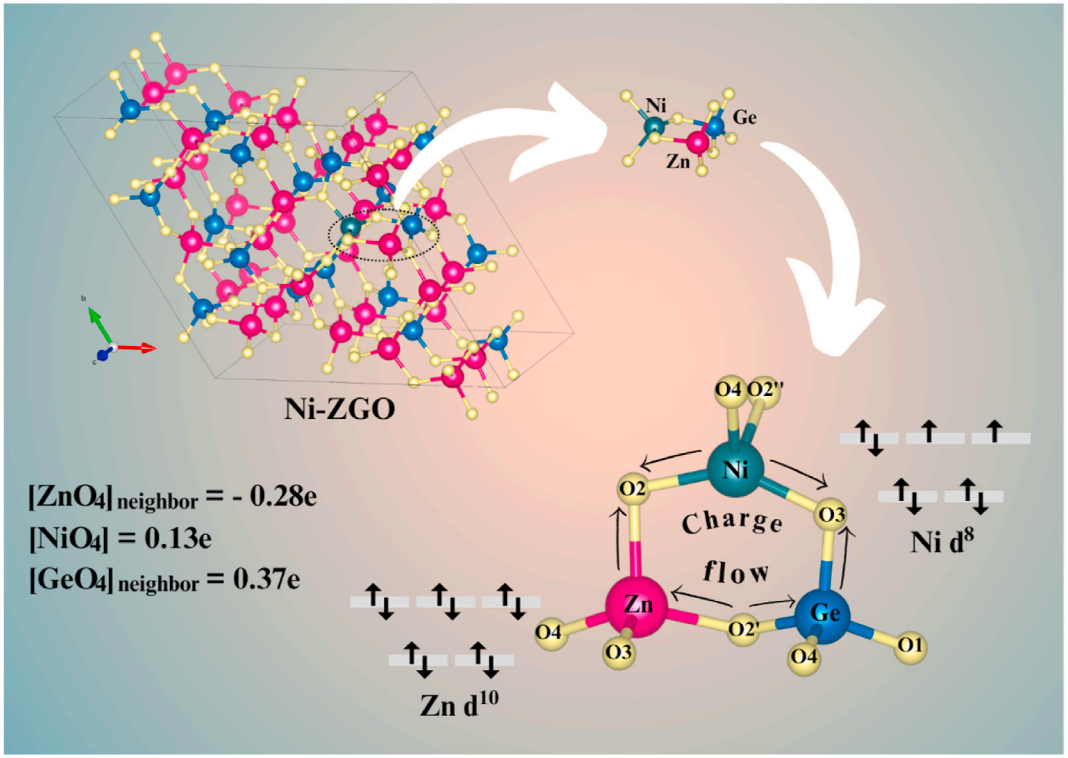

Fig. 7. Schematic representation of the $[NO_4]$, neighbor $[ZnO_4]$ (at the six-membered rings composed only by Zn2 sites) and $[GeO_4]$ (at the six-membered rings composed by Z1 sites and Ge). Values of the Mulliken charges and the respective metal electronic configuration induced by the Ni^{2+}-doping process.

in developing NIR reflective pigments.

The color of the samples was determined using the CIELab colorimetric method. The photos of the powders obtained in this work are shown in Fig. S9. This CIELab color space, standardized by the Commission Internationale d'Eclairage, identifies colors in a 3D model composed of coordinates [65]. The coordinates a* and b* are related to colors such as yellow (-b*), blue (b*), green (-a*), and red (a*). In contrast, the L* coordinate indicates the brightness of the color, ranging from 0, representing a material towards black, to 100 for lighter materials close to white. Analyzing Fig. 9a and the data in Table 3, it can be observed that the ZGO, ZGO1, and ZGO-1000 pigments showed slight differences in the values of the -a* and -b* coordinates, indicating a subtle change in the color of the pure pigment and when doped with low amounts of Ni^{2+} without thermal treatment. The ZGO16 sample appears with a light green hue, with a* and b* coordinates of -10.07 ± 0.011 and 5.30 ± 0.024, respectively. Upon calcination of the samples at 1000 °C, ZGO1-1000 and ZGO16-1000 undergo significant variations in hue. The ZGO1-1000 sample appears as a purer blue pigment, with a* and b* coordinates of 2.73 ± 0.087 and -28.00 ± 1.050, while the increased concentration of Ni^{2+} in the ZGO16-1000 sample results in obtaining a pigment with a greenish blue color, with a* and b* coordinates of -13.61 ± 0.009 and -11.58 ± 0.089. It is important to note that intermediate concentrations between 0.16 % and 0.01 % were tested, which do not show changes in their hues compared to the ZGO1-1000 sample (see Fig. S10 and Table S5). Additionally, a decrease in the brightness of the thermally treated pigments is noticeable as they are doped (Fig. 9b).

Ahmed et al. conducted a study on blue pigments, where the doping of Ni^{2+} in $MgAl_2O_4$ resulted in a reduction in the brightness of the doped samples as the concentration of Ni^{2+} increased [66]. Additionally, the increase in temperature also led to changes in the values of a* and b*, with an increase towards the depth of the green-blue color. Blue pigments based on $Ca_{1-x}La_xAl_{12-x}Ni_xO_{19}$ were obtained by coupled substitution $(Ca^{2+} + Al^{3+}) \rightarrow (La^{3+} + Ni^{2+})$ in the hibonite structure by Ianos et al. [27] Ni^{2+}-doped samples exhibited negative values of a* and b*, indicating a bluish-green hue. Increasing the Ni^{2+} content intensified the blue color, as confirmed by the decrease in b* and L* values. Wang et al. obtained blue pigments based on V–$ZrSiO_4$ calcined at 1100 °C for 1 h

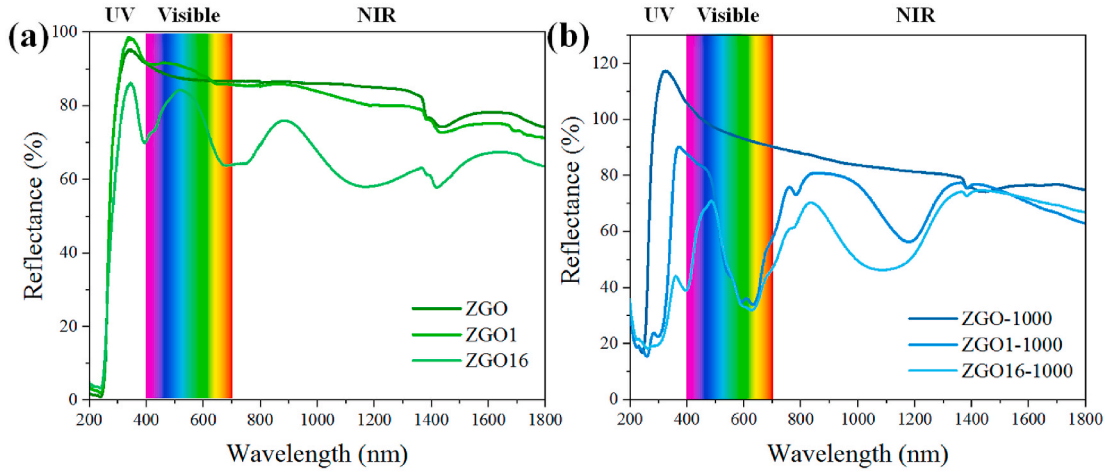

Fig. 8. Spectra of absorption in the UV–Vis and NIR regions for the samples **a)** untreated and **b)** thermally treated.

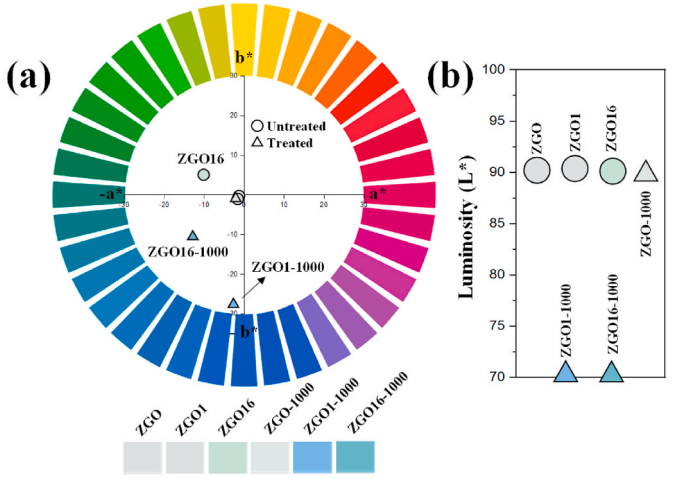

Fig. 9. (a) a* (green and red), b* (yellow and blue) and **(b)** and L* (lightness, with 100 representing white and 0 representing black) CIELab coordinates for the samples. (For interpretation of the references to color in this figure legend, the reader is referred to the Web version of this article.)

[5]. While the pure sample exhibited a white color, those containing vanadium showed a more intense blue hue, with reduced L* and b* values. Increasing the vanadium concentration resulted in a decrease in L* and b*. Notably, the sample with 2 % vanadium exhibited the brightest blue color. These findings suggest that controlled addition of vanadium can enhance the quality of the pigment for specific applications. In this work, the observed difference in coloration is attributed to two factors: (1) a more significant contribution of charge transfer between O, Zn, and Ni, as evidenced in the analysis of the DRS spectra, and (2) the difference in coordination of Ni^{2+} clusters, which are in octahedral sites in the NiO and $Zn_{0.2}Ni_{0.8}GeO_4$ phases, and tetrahedral sites when acting as dopants in Zn_2GeO_4 phase, corroborating with the obtained theoretical results [63].

As previously mentioned, the d-d transitions of the Ni^{2+} cation in a tetrahedral symmetry play a crucial role in the origin of the observed blue coloration. Under the influence of crystal field theory, the 5 d orbitals of the Ni^{2+} cation experience an energy separation due to interaction with surrounding oxygen atoms in a tetrahedral environment. In this context, d-d transitions occur when electrons are excited between the energy levels of the orbitals [27]. The Jahn-Teller effect, in turn, contributes to the system's complexity by promoting a geometric distortion that breaks the tetrahedral symmetry [22]. This distortion is particularly significant for Ni^{2+} cations in tetrahedral environments, influencing their spectral and magnetic properties. An analysis of the DOS renders that 3d orbitals of the Ni^{2+} cation is non-degenerate, been the $3d_{x^2-y^2}$ orbital the most energetic at the top of VB. However, it is essential to note the limitations of the present strategy, which focuses on the local environment without considering the complexity of the entire system.

4. Conclusions

A coprecipitation method followed by microwave-assisted hydrothermal treatment has been first applied for producing blue nickel Ni^{2+}-doped Zn_2GeO_4 (x = 0–0.16 mol%) pigments. Doping with Ni^{2+} at low concentrations (x = 0.01 %) resulted in the pure rhombohedral phase of Zn_2GeO_4. However, at higher Ni^{2+} concentrations (x = 0.08 and 0.16 %), the coexistence of additional phases, NiO (~3 %) and $Zn_{1.2}Ni_{0.8}GeO_4$ (~8 %) was observed. XPS analysis revealed that thermal treatment can also alter the material surface. The substitution of Zn^{2+} by Ni^{2+} at x = 0.01 % directionally regulates the electron redistribution, likely

Table 3
The samples' colorimetric parameters (L*, a*, b*, color).

Sample	a*	b*	L*	Color
ZGO2	-2.44 ± 0.027	-0.06 ± 0.029	91.38 ± 0.023	
ZGO4	-3.15 ± 0.030	-0.56 ± 0.051	90.75 ± 0.062	
ZGO8	-5.74 ± 0.016	-2.08 ± 0.011	90.08 ± 0.024	
ZGO2-1000	-2.39 ± 0.040	-29.35 ± 0.185	71.26 ± 0.022	
ZGO4-1000	-4.84 ± 0.014	-25.52 ± 0.136	70.37 ± 0.054	
ZGO8-1000	-4.83 ± 0.005	-12.21 ± 0.045	77.99 ± 0.074	

occurring from [NiO_4] to tetrahedral [ZnO_4] and [GeO_4] neighbor clusters, which is responsible for the observed blue color, as confirmed by colorimetric and spectroscopic analysis and density functional theory (DFT) calculations. In this regard, lower concentrations of Ni^{2+} (between 0.01, 0.02, and 0.04 %) are capable of producing blue pigments, whereas higher concentrations start to produce greenish blue pigments due to the formation of clusters [NiO_8] originating from additional phases. The substitution of Zn^{2+} by Ni^{2+} at x = 0.01 % directionally regulates the electron transfer, likely occurring from [NiO_4] and tetrahedral [ZnO_4] and [GeO_4] neighbor clusters to shared oxygen anions. Furthermore, adding Ni^{2+} enables absorptions in the NIR region, which is particularly valuable for obtaining reflective pigments. These findings provided a new idea for the design of novel Ni^{2+}-doped Zn_2GeO_4 to meet diverse application needs.

CRediT authorship contribution statement

Katiana L. Patrocínio: Writing – original draft, Methodology, Investigation, Formal analysis, Data curation. **Gleison N. Marques:** Writing – review & editing, Writing – original draft, Methodology, Investigation, Formal analysis, Data curation. **Amanda F. Gouveia:** Writing – review & editing, Writing – original draft, Methodology, Formal analysis, Data curation. **Lara K. Ribeiro:** Writing – review & editing, Writing – original draft, Investigation, Formal analysis, Data curation. **Nayara A. Pinheiro:** Methodology, Investigation, Formal analysis, Data curation. **Maria I.B. Bernardi:** Writing – original draft, Methodology, Investigation, Formal analysis, Data curation. **Lúcia H. Mascaro:** Writing – review & editing, Project administration, Funding acquisition, Data curation. **Juan Andrés:** Writing – review & editing, Validation, Resources, Project administration. **Elson Longo:** Writing – review & editing, Validation, Resources, Project administration. **Marcelo Assis:** Writing – review & editing, Writing – original draft, Visualization, Validation, Supervision, Resources, Project administration, Methodology, Investigation, Funding acquisition, Formal analysis, Data curation, Conceptualization.

Declaration of competing interest

The authors declare that they have no known competing financial interests or personal relationships that could have appeared to influence the work reported in this paper.

Acknowledgments

This work was funded in part by Fundação de Amparo à Pesquisa do Estado de São Paulo – FAPESP (FAPESP CEPID-finance code 2013/07296-2, 2021/06128-5), Financiadora de Estudos e Projetos – FINEP, Conselho Nacional de Desenvolvimento Científico e Tecnológico – CNPq, and Coordenação de Aperfeiçoamento de Pessoal de Nível Superior – CAPES (finance code 001). A.F.G. acknowledges the Generalitat Valenciana (Conselleria de Innovación, Universidades, Ciencia y Sociedad Digital) for the postdoctoral contract (CIAPOS/2021/106). L.K.R. thanks the São Paulo Research Foundation and CNPq (FAPESP, grant #2023/12399-7; CNPq, grant #158689/2023-2). J.A. acknowledges Ministerio de Ciencia, Innovación y Universidades (Spain) (project PGC2018094417-B-I00), Generalitat Valenciana (Conselleria de Innovación, Universidades, Ciencia y Sociedad Digital – project CIAICO/2021/122) and Jaume I University (UJI-B2022-56) for financially supporting this research. M.A. was supported by the Margarita Salas postdoctoral contract MGS/2021/21 (UP2021-021) financed by the European Union-Next Generation EU.

Appendix A. Supplementary data

Supplementary data to this article can be found online at https://doi.org/10.1016/j.ceramint.2024.05.493.

References

[1] M. Llusar, A. Forés, J.A. Badenes, J. Calbo, M.A. Tena, G. Monrós, Colour analysis of some cobalt-based blue pigments, J. Eur. Ceram. Soc. 21 (2001) 1121–1130, https://doi.org/10.1016/S0955-2219(00)00295-8.

[2] K. Zheng, F. Yang, Z. Huang, Y. Zhan, Z. Xiao, W. Li, W. Wang, C. Qin, Preparation of chitosan film-loaded palladium catalyst materials and their application in Suzuki coupling reactions, J. Mater. Res. Technol. 20 (2022) 3905–3917, https://doi.org/10.1016/j.jmrt.2022.08.130.

[3] J. Jing, Y. Zhang, J. Sun, X. Zhao, D. Gao, Y. Zhang, A comparative study on different RE-doped (RE=Pr, Nd, Sm) $SrCuSi_4O_{10}$ blue pigments with high near-infrared reflectance, Dyes Pigments 150 (2018) 9–15, https://doi.org/10.1016/j.dyepig.2017.10.045.

[4] A.E. Smith, H. Mizoguchi, K. Delaney, N.A. Spaldin, A.W. Sleight, M. A. Subramanian, Mn^{3+} in trigonal bipyramidal coordination: a new blue chromophore, J. Am. Chem. Soc. 131 (2009) 17084–17086, https://doi.org/10.1021/ja9080666.

[5] T. Wang, J. Liu, W. Jiang, F. Jiang, G. Feng, L. Miao, Q. Zhang, Q. Wu, X. Lao, Fluorine-free synthesis and characterization of vanadium-zircon (V–$ZrSiO_4$) turquoise ceramic pigment by a low temperature solid state reaction route, Ceram. Int. 48 (2022) 24044–24055, https://doi.org/10.1016/j.ceramint.2022.05.083.

[6] E. Ozel, H. Yurdakul, S. Turan, M. Ardit, G. Cruciani, M. Dondi, Co-doped willemite ceramic pigments: technological behaviour, crystal structure and optical properties, J. Eur. Ceram. Soc. 30 (2010) 3319–3329, https://doi.org/10.1016/j.jeurceramsoc.2010.08.013.

[7] M. Benchikhi, R. Hattaf, A. Moutaabbid, R. El Ouatib, Structural, morphological, and optical properties of Co- substituted Zn2SiO4 nanopowders prepared by a hydrothermal-assisted sol-gel process, Mater. Chem. Phys. 276 (2022) 125434, https://doi.org/10.1016/j.matchemphys.2021.125434.

[8] J. Liang, J. Xu, J. Long, Z. Zhang, X. Wang, Self-assembled micro/nano-structured Zn_2GeO_4 hollow spheres: direct synthesis and enhanced photocatalytic activity, J. Mater. Chem. A 1 (2013) 10622–10625, https://doi.org/10.1039/C3TA12183F.

[9] Y. Li, A. Zhao, C. Chen, C. Zhang, J. Zhang, G. Jia, Controllable synthesis and morphology-dependent photoluminescence properties of well-defined one-dimensional Zn_2GeO_4:Mn^{2+} nanostructures, Dyes Pigments 150 (2018) 267–274, https://doi.org/10.1016/j.dyepig.2017.12.021.

[10] K. Lin, B. Ma, W. Su, W. Liu, Improved photocatalytic hydrogen generation on Zn_2GeO_4 nanorods with high crystallinity, Appl. Surf. Sci. 286 (2013) 61–65, https://doi.org/10.1016/j.apsusc.2013.09.014.

[11] Y. Zhao, S. Feng, H. Jiang, S. Ma, Z. Tao, W. Lu, Y. Fan, Catalyst-free growth of a Zn_2GeO_4 nanowire network for high-performance transfer-free solar-blind deep UV detection, Phys. E Low-Dimensional Syst. Nanostructures. 107 (2019) 1–4, https://doi.org/10.1016/j.physe.2018.11.015.

[12] V.B.R. Boppana, N.D. Hould, R.F. Lobo, Synthesis, characterization and photocatalytic properties of novel zinc germanate nano-materials, J. Solid State Chem. 184 (2011) 1054–1062, https://doi.org/10.1016/j.jssc.2011.02.022.

[13] J.P.A. de Jesus, A.C.L. Santos, F.M. Pinto, C.A. Taft, F.A. La Porta, Review: theoretical and experimental investigation of the intrinsic properties of Zn_2GeO_4 nanocrystals, J. Mater. Sci. 56 (2021) 4552–4568, https://doi.org/10.1007/s10853-020-05549-8.

[14] J. Dolado, J. García-Fernández, P. Hidalgo, J. González-Calbet, J. Ramírez-Castellanos, B. Méndez, Intense cold-white emission due to native defects in Zn_2GeO_4 nanocrystals, J. Alloys Compd. 898 (2022) 162993, https://doi.org/10.1016/j.jallcom.2021.162993.

[15] J. Dolado, B. Rodríguez, R. Martínez-Casado, I. Píš, E. Magnano, P. Hidalgo, B. Méndez, Li-doping effects on the native defects and luminescence of Zn_2GeO_4 microstructures: negative thermal quenching, Acta Mater. 245 (2023), https://doi.org/10.1016/j.actamat.2022.118606.

[16] S.K. Gupta, K. Sudarshan, B. Modak, R. Gupta, Interstitial zinc boosted light tunability, afterglow, and ultrabright white emission in zinc germanate (Zn_2GeO_4), ACS Appl. Electron. Mater. 5 (2023) 1286–1294, https://doi.org/10.1021/acsaelm.2c01759.

[17] M.T.A. Balhara, S.K. Gupta, M. Abraham, B. Modak, S. Das, C. Nayak, H. V. Annadata, Trap engineering through chemical doping for ultralong X-ray persistent luminescence and anti-thermal quenching in Zn_2GeO_4, J. Mater. Chem. C 12 (2024) 1718–1727, https://doi.org/10.1039/D3TC03442A.

[18] F. Gao, Q. Pang, D. Gao, C. Jia, H. Xin, Y. Pan, Y. Wang, S. Yun, Mn^{2+}-Activated photostimulable persistent nanophosphors by Pr^{3+} codoping for rewritable information storage, ACS Appl. Nano Mater. 6 (2023) 3054–3064, https://doi.org/10.1021/acsanm.2c05552.

[19] B.B. Srivastava, S.K. Gupta, Y. Li, Y. Mao, Bright persistent green emitting water-dispersible Zn_2GeO_4:Mn nanorods, Dalton Trans. 49 (2020) 7328–7340, https://doi.org/10.1039/d0dt00361a.

[20] F. Chi, B. Jiang, Z. Zhao, Y. Chen, X. Wei, C. Duan, M. Yin, W. Xu, Multimodal temperature sensing using Zn_2GeO_4:Mn^{2+} phosphor as highly sensitive luminescent thermometer, Sensor. Actuator. B Chem. 296 (2019) 1–8, https://doi.org/10.1016/j.snb.2019.126640.

[21] N.M. Cao Hoang Phuong Lan, C.X. Thang, V.H. Pham, P. The Kien, V.T. Ngoc Minh, T.T. Hao Tam, Effects of Cr-doping on the morphology and optical properties in Zn_2GeO_4 (ZGO) nanorods prepared by hydrothermal method, Optik 199 (2019) 163310, https://doi.org/10.1016/j.ijleo.2019.163310.

[22] A.K.V. Raj, P.P. Rao, Intense blue chromophores in cobalt doped phenacite-type zinc germanate system through Jahn-Teller distortion of Co Tetrahedron, ChemistrySelect 6 (2021) 11344–11351, https://doi.org/10.1002/slct.202102998.

[23] N. Gorodylova, V. Kosinová, Ž. Dohnalová, P. Bělina, P. Šulcová, New purple-blue ceramic pigments based on $CoZr_4(PO_4)_6$, Dyes Pigments 98 (2013) 393–404, https://doi.org/10.1016/j.dyepig.2013.03.004.

[24] S.H. Farjana, N. Huda, M.A.P. Mahmud, Life cycle assessment of cobalt extraction process, J. Sustain. Min. 18 (2019) 150–161, https://doi.org/10.1016/j.jsm.2019.03.002.

[25] A. Schedle, P. Samorapoompichit, X.H. Rausch-Fan, A. Franz, W. Füreder, W. R. Sperr, W. Sperr, A. Ellinger, R. Slavicek, G. Boltz-Nitulescu, P. Valent, Response of L-929 fibroblasts, human gingival fibroblasts, and human tissue mast cells to various metal cations, J. Dent. Res. 74 (1995) 1513–1520, https://doi.org/10.1177/00220345950740081301.

[26] G. Schmalz, D. Arenholt-Bindslev, S. Pfüller, H. Schweikl, Cytotoxicity of metal cations used in dental cast alloys, Altern. Lab. Anim. 25 (1997) 323–330, https://doi.org/10.1177/026119299702500313.

[27] R. Ianoș, I. Rus, R. Lazău, C. Păcurariu, Near-infrared reflective Ni, La-doped hibonite pigments for cool blue coatings, Ceram. Int. 48 (2022) 34428–34436, https://doi.org/10.1016/j.ceramint.2022.08.021.

[28] J. Chen, G. Feng, F. Jiang, L. Yin, Q. Zhao, S. Lan, X.J. Zhang, J. Liu, Q. Hu, W. Jiang, Synthesis and coloring properties of novel Ni-doped tialite pigments, Ceram. Int. 47 (2021) 33242–33251, https://doi.org/10.1016/j.ceramint.2021.08.225.

[29] Y. Wang, P. Jiang, M.A. Subramanian, W. Cao, Synthesis, properties and applications of novel inorganic yellow pigments based on Ni-doped Al_2TiO_5, Solid State Sci. 135 (2023) 107088, https://doi.org/10.1016/j.solidstatesciences.2022.107088.

[30] Q. Wang, Z. Wang, M. Qi, H. Zhao, X. Xin, A. Verma, T. Siritanon, A.P. Ramirez, M. A. Subramanian, P. Jiang, Synthesis and optical properties based on Ni-doped Zn_2SiO_4 blue pigments with high-NIR reflectance, ACS Sustain. Chem. Eng. 12 (2024) 5522–5532, https://doi.org/10.1021/acssuschemeng.3c07982.

[31] G. Costa, M.J. Ribeiro, W. Hajjaji, M.P. Seabra, J.A. Labrincha, M. Dondi, G. Cruciani, Ni-doped hibonite ($CaAl_{12}O_{19}$): a new turquoise blue ceramic pigment, J. Eur. Ceram. Soc. 29 (2009) 2671–2678, https://doi.org/10.1016/j.jeurceramsoc.2009.04.001.

[32] M. Khairy, N. Magdy, Z.A. Omran, Effect of Ni content, temperature on the electrical and colorimetric properties of nano $Ni_xZn_{(1-x)}O$ blue pigments, Dig. J. Nanomater. Biostruct. 17 (2022) 1111–1124, https://doi.org/10.15251/DJNB.2022.173.1111.

[33] V.Y. Suzuki, N.H. de Paula, R. Gonçalves, M.S. Li, E.C. Pereira, E. Longo, F.A. La Porta, Exploring effects of microwave-assisted thermal annealing on optical properties of Zn_2GeO_4 nanostructured films, Mater. Sci. Eng. B. 246 (2019) 7–12, https://doi.org/10.1016/j.mseb.2019.05.023.

[34] V.Y. Suzuki, L.H.C. Amorin, N.M. Lima, E.G. Machado, P.E. Carvalho, S.B. R. Castro, C.C.S. Alves, A.P. Carli, M.S. Li, E. Longo, F.A. La Porta, Characterization of the structural, optical, photocatalytic and in vitro and in vivo anti-inflammatory properties of Mn^{2+} doped Zn_2GeO_4 nanorods, J. Mater. Chem. C 7 (2019) 8216–8225, https://doi.org/10.1039/C9TC01189G.

[35] R. Dovesi, R. Orlando, A. Erba, C.M. Zicovich-Wilson, B. Civalleri, S. Casassa, L. Maschio, M. Ferrabone, M. De La Pierre, P. D'Arco, Y. Noël, M. Causà, M. Rérat, B. Kirtman, C RYSTAL14: a program for the ab initio investigation of crystalline solids, Int. J. Quant. Chem. 114 (2014) 1287–1317, https://doi.org/10.1002/qua.24658.

[36] R. Dovesi, V.R. Saunders, C. Roetti, R. Orlando, C.M. Zicovich-Wilson, F. Pascale, B. Civalleri, K. Doll, N.M. Harrison, I.J. Bush, P. D'Arco, M. Llunel, M. Causà, Y. Noël, L. Maschio, A. Erba, M. Rérat, S. Casassa, CRYSTAL14 user's manual, Theor. Chem. Group, Univ. Turin Italy (2014) 211.

[37] A.D. Becke, Density-functional thermochemistry. III. The role of exact exchange, J. Chem. Phys. 98 (1993) 5648–5652, https://doi.org/10.1063/1.464913.

[38] R.G. Lee, C. Yang, W. Parr, Development of the Colic-Salvetti correlation-energy formula into a functional of the electron density, Phys. Rev. B Condens. Matter 37 (1988) 785–789.

[39] Crystal. http://www.crystal.unito.it/Basis_Sets/Ptable.html.

[40] J. Dolado, R. Martínez-Casado, P. Hidalgo, R. Gutierrez, A. Dianat, G. Cuniberti, F. Domínguez-Adame, E. Díaz, B. Méndez, Understanding the UV luminescence of zinc germanate: the role of native defects, Acta Mater. 196 (2020) 626–634, https://doi.org/10.1016/j.actamat.2020.07.009.

[41] Z.Y. Xie, H.L. Lu, Y. Zhang, Q.Q. Sun, P. Zhou, S.J. Ding, D.W. Zhang, The electronic structures and optical properties of Zn_2GeO_4 with native defects, J. Alloys Compd. 619 (2015) 368–371, https://doi.org/10.1016/j.jallcom.2014.09.003.

[42] J. Huang, K. Ding, Y. Hou, X. Wang, X. Fu, Synthesis and photocatalytic activity of Zn_2GeO_4 nanorods for the degradation of organic pollutants in water, ChemSusChem 1 (2008) 1011–1019, https://doi.org/10.1002/cssc.200800166.

[43] J. Breternitz, D. Fritsch, A. Franz, S. Schorr, A thorough investigation of the crystal structure of willemite-type Zn_2GeO_4, Zeitschrift Fur Anorg. Und Allg, Chemie 647 (2021) 2195–2200, https://doi.org/10.1002/zaac.202100231.

[44] L. Liu, X. Zhao, H. Sun, C. Jia, W. Fan, Theoretical study of H_2O adsorption on Zn_2GeO_4 surfaces: effects of surface state and structure-activity relationships, ACS Appl. Mater. Interfaces 5 (2013) 6893–6901, https://doi.org/10.1021/am4015692.

[45] Y. Zhao, S. Yang, J. Zhu, G. Ji, F. Peng, The study of oxygen ion motion in Zn_2GeO_4 by Raman spectroscopy, Solid State Ionics 274 (2015) 12–16, https://doi.org/10.1016/j.ssi.2015.02.015.

[46] D.K. Bharti, S. Badatya, P. Tanwar, J. Tawale, A.K. Srivastava, M.K. Gupta, Observation of anomalous phase transition and band gap shrinkage in zinc germanate nanorods, Mater. Sci. Eng. B. 259 (2020) 114602, https://doi.org/10.1016/j.mseb.2020.114602.

[47] P. Hidalgo, A. López, B. Méndez, J. Piqueras, Synthesis and optical properties of Zn_2GeO_4 microrods, Acta Mater. 104 (2016) 84–90, https://doi.org/10.1016/j.actamat.2015.11.023.

[48] J.I. Viegas, R.L. Moreira, A. Dias, Optical-vibration and intrinsic dielectric properties of low-k high-Q Zn_2GeO_4 ceramics, J. Phys. Chem. Solid. 148 (2021), https://doi.org/10.1016/j.jpcs.2020.109693.

[49] J. Liu, G. Zhang, Template-free synthesis and high photocatalytic activity of hierarchical Zn_2GeO_4 microspheres, CrystEngComm 15 (2013) 382–389, https://doi.org/10.1039/c2ce26316e.

[50] O. Yamaguchi, J. Hidaka, K. Hirota, Formation and characterization of alkoxy-derived Zn_2GeO_4, J. Mater. Sci. Lett. 10 (1991) 1471–1474, https://doi.org/10.1007/BF00724409.

[51] S. Cui, Y. Jiao, J. Liu, Y. Pu, J.X. Wang, D. Wang, High-gravity-driven process intensified approach toward Mn^{2+} doped Zn_2GeO_4 nanophosphors for deep-ultraviolet detecting, Optik 235 (2021) 166644, https://doi.org/10.1016/j.ijleo.2021.166644.

[52] T. Han, C. Li, W. Zhao, Y. She, J. Jiao, F. Liang, Z. Hu, Y. Wu, Investigations on the synthesis, crystal structure, linear- and nonlinear-optical properties of the zinc germanate $Rb_2ZnGe_2O_6$, Inorg. Chem. 61 (2022) 706–712, https://doi.org/10.1021/acs.inorgchem.1c03465.

[53] S. Wu, Q. Ma, Synthesis, characterization and microwave dielectric properties of Zn_2GeO_4 ceramics, J. Alloys Compd. 567 (2013) 40–46, https://doi.org/10.1016/j.jallcom.2013.03.052.

[54] H. He, Y. Zhang, Q. Pan, G. Wu, G. Dong, J. Qiu, Controllable synthesis of Zn_2GeO_4: Eu nanocrystals with multi-color emission for white light-emitting diodes, J. Mater. Chem. C 3 (2015) 5419–5429, https://doi.org/10.1039/c5tc00844a.

[55] C. Guo, S. Chen, J. Aslam, J. Li, L.P. Lv, W. Sun, W. Cao, Y. Wang, Microwave-assisted metal-organic frameworks derived synthesis of Zn_2GeO_4 nanowire bundles for lithium-ion batteries, Nanomaterials 13 (2023), https://doi.org/10.3390/nano13081432.

[56] F. Zou, X. Hu, L. Qie, Y. Jiang, X. Xiong, Y. Qiao, Y. Huang, Facile synthesis of sandwiched Zn_2GeO_4-graphene oxide nanocomposite as a stable and high-capacity anode for lithium-ion batteries, Nanoscale 6 (2014) 924–930, https://doi.org/10.1039/c3nr04917e.

[57] A. Ohta, H. Nakagawa, H. Murakami, S. Higashi, S. Miyazaki, Photoemission study of ultrathin GeO_2/Ge heterostructures formed by UV-O_3 oxidation, E-Journal Surf. Sci. Nanotechnol. 4 (2006) 174–179, https://doi.org/10.1380/ejssnt.2006.174.

[58] Z. Ma, X. Liu, X. Wang, Z. Luo, W. Li, Y. Nie, L. Pei, Q. Mao, X. Wen, J. Zhong, Manipulating the d-band center enhances photoreduction of CO_2 to CO in Zn_2GeO_4 nanorods, Chem. Eng. J. 468 (2023) 143569, https://doi.org/10.1016/j.cej.2023.143569.

[59] B. Kalita, S. Iraqui, X. Borgohain, M.H. Rashid, Ultrasonic irradiation-assisted $MnFe_2O_4$ nanoparticles catalyzed solvent-free selective oxidation of benzyl alcohol to benzaldehyde at room temperature, RSC Adv. 13 (2023) 30855–30868, https://doi.org/10.1039/d3ra03797e.

[60] X. Chen, X. Sha, Y. Zhang, D. Gao, L. Wang, Y. Zhang, T. Liu, X. Zhang, J. Zhang, Y. Cao, Y. Wang, X. Li, S. Xu, H. Yu, B. Chen, Multicolor-emitting Er^{3+} and Er^{3+}/Yb^{3+} doped Zn_2GeO_4 phosphors combining static and dynamic identifications for advanced anti-counterfeiting application, Spectrochim. Acta Part A Mol. Biomol. Spectrosc. 309 (2024) 123830, https://doi.org/10.1016/j.saa.2023.123830.

[61] P. Kubelka, F. Munk, Ein Beitrag Zur Optik Der Farbanstriche, Zeitschrift Für Tech. Phys. 12 (1931) 593–601.

[62] J. Sato, H. Kobayashi, K. Ikarashi, N. Saito, H. Nishiyama, Y. Inoue, Photocatalytic activity for water decomposition of RuO_2-dispersed Zn_2GeO_4 with d10 configuration, J. Phys. Chem. B 108 (2004) 4369–4375, https://doi.org/10.1021/jp0373189.

[63] M. Gaudon, L.C. Robertson, E. Lataste, M. Duttine, M. Ménétrier, A. Demourgues, Cobalt and nickel aluminate spinels: blue and cyan pigments, Ceram. Int. 40 (2014) 5201–5207, https://doi.org/10.1016/j.ceramint.2013.10.081.

[64] S. Zhang, Z. Pan, Y. Wang, Synthesis and characterization of (Ni, Sb)-co-doped rutile ceramic pigment via mechanical activation-assisted solid-state reaction, Particuology 41 (2018) 20–29, https://doi.org/10.1016/j.partic.2017.12.016.

[65] C. Arc, E. Lamps, Encyclopedia of Color Science and Technology, 2016, https://doi.org/10.1007/978-1-4419-8071-7.

[66] I.S. Ahmed, H.A. Dessouki, A.A. Ali, Synthesis and characterization of $Ni_xMg_{1-x}Al_2O_4$ nano ceramic pigments via a combustion route, Polyhedron 30 (2011) 584–591, https://doi.org/10.1016/j.poly.2010.11.034.